Observation and mechanism of local oxygen reordering induced by high-energy heavy-ion (U^+, Au^+, Xe^+) irradiation in the high-T_c superconductor $YBa_2Cu_3O_{7-\delta}$

Y. Yan and M. A. Kirk
Materials Science Division, Argonne National Laboratory, Argonne, Illinois 60439
(Received 8 September 1997; revised manuscript received 7 November 1997)

Transmission electron microscopy study reveals that high-energy (>1 GeV) heavy-ion (U^+, Au^+, Xe^+) irradiation in the c-axis direction of high-T_c superconductor $YBa_2Cu_3O_{7-\delta}$ leads to the formation of aligned columnar defects, which are usually amorphous, and the associated volume expansion causes strain in surrounding matrix. Lobed ''bow-tie'' contrast is observed in both the [001] zone axis bright field and the high-resolution images of the regions surrounding the amorphous columns, the direction of which is rotated 90° across a typical pre-existing twin boundary in $YBa_2Cu_3O_{7-\delta}$. Our study shows that this contrast is caused by local oxygen reordering in the ab planes that gives a 90° reorientation of the orthorhombic unit cell in the affected area. The mechanism of resulting oxygen reordering in the ab planes for this area is reported here. A qualitative result on the form, the position, and the size of the oxygen reordering region distributed around an isolated track and between two or more tracks, is related to the orientation of the Cu-O chain direction of matrix and the energy of incident ions. [S0163-1829(98)04010-7]

I. INTRODUCTION

It is well known that a high critical current density J_c can be obtained in high-T_c superconductors only if vortices in the sample are prevented from moving by being pinned on microscopic defects comparable in size to the superconducting coherence length that determines the vortex core radius. Heavy-ion irradiation is a well-established method for the controlled introduction of pinning defects in high-temperature superconductors in a manner that does not significantly affect the mean-field superconducting parameters, including the transition temperature T_c. Clearly, investigation of correlation between changes in superconducting properties and the damaged microstructure is essential if the detailed mechanisms of the pinning behavior are to be understood. Recently several groups have studied the influence of structural defects created by heavy-ion irradiation of differing energies on the J_c of high-T_c $YBa_2Cu_3O_{7-\delta}$ (YBCO) material.[1–8] The ion-induced defects are generally considered to be continuous cylinders[5] of amorphized material with cylindrically symmetric strain fields around them.[8] Welch and co-workers[9] have pointed out that the detailed interpretation of transport data in heavy-ion irradiated crystals requires an understanding of the defects and strains around the columns. In this context a quantitative study was made on the strain fields around the reportedly cylindrical amorphous columns formed by c-axis Au ion irradiation at 300 MeV.[8] The work, while making a significant contribution to the understanding of irradiation damage, ignores possible effects due to orthorhombicity. As we show here, this is of central importance in the interpretation of the effects of the still higher energy (>1 GeV) c-axis heavy-ion irradiation of YBCO. Here, we present a systematic investigation of the irradiation damage induced by various heavy ions (U^+, Au^+, and Xe^+) with different energies (1.3–2.29 GeV) by means of transmission electron microscopy (TEM). The contrast of the damaged area was studied in both the [001] high-resolution image and the zone axis bright field (ZABF) image by which the contrast of defects, particularly from the oxygen reordering (ORO) around the damaged tracks in the orthorhombic $YBa_2Cu_3O_{7-\delta}$ system, can be enhanced. The mechanism of resulting oxygen reordering in the ab planes is presented.

II. EXPERIMENTAL PROCEDURE

Single crystal YBCO samples ($T_c \sim 92$ K) were irradiated by various heavy ions at room temperature at the ATLAS heavy-ion accelerator in Argonne, the NSCL heavy-ion accelerator of Michigan State University, and the UNILAC heavy-ion accelerator in Darmstadt, with the irradiation nominally perpendicular to the specimen surface (nearly parallel to the c axis). A flux of $4 \sim 8 \times 10^7$ ions $cm^{-2}\,s^{-1}$ was used to avoid beam heating effects. Details about the energy, dose of the incident ions are given in Table I. TEM samples were made by two different methods: prethinned foil and crushed (or ion-milled) bulk sample. The sample YY01 was prethinned by ion milling: nonirradiated single-crystal YBCO specimens were first thinned using ~ 4 kV argon ion milling with liquid-nitrogen cooling to produce a wedge specimen that could be examined by TEM after it had been

TABLE I. Irradiation conditions for the three irradiated single crystals of $YBa_2Cu_3O_{7-\delta}$ examined in this work.

Sample number	Ion	Z	Ion energy (GeV)	Dose (ion/cm^2)	Facilities
WMU 2003-2	U	92	1.3	2.4×10^{10}	(ATLAS) Argonne
LPB-2	Xe	54	2.29	2.4×10^{10}	(NSCL) Michigan State University
YY-01	Au	79	2.25	2.0×10^{10}	(UNILAC) Darmstadt

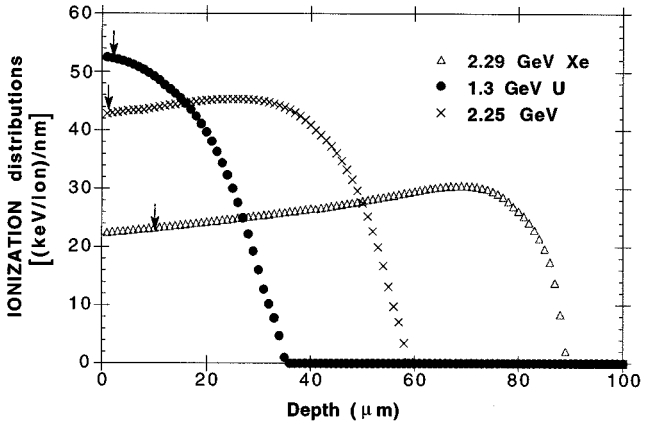

FIG. 1. Calculations from TRIM 90 showing the variation of the energy loss as a function of penetration depth for Au, U, and Xe ions in $YBa_2Cu_3O_{7-\delta}$. Arrows indicate approximate depths of TEM examinations.

damaged by the subsequent passage of high-energy ions. The damage was then examined by TEM after removing approximately 100 nm from the top surface of the crystal using low-energy argon ion milling. The second way for preparing TEM samples in this study is mechanically crushing (sample WMU2003-2) or ion milling (samples LPB-2 and WMU2003-2) the irradiated bulk sample. A reliable method for crushing very small brittle crystals was established by Frischherz *et al.*[10] while investigating neutron irradiation damage in YBCO. This enables one to gently crush a small crystal in just a few drops of methanol. After the crystal is crushed, the powder, suspended in fresh anhydrous methanol, is extracted via a pipette and then dispersed onto a clean 1000 mesh TEM grid. The depths from top surface of our samples used for TEM examinations here are at $\sim 3\ \mu$m for the U^+, $\sim 10\ \mu$m for the Xe^+, and $<1\ \mu$m for the Au^+ irradiation. Calculations using TRIM Monte Carlo energy deposition routine,[17] which show that the mean electronic energy loss of these three ions varies with the depth in YBCO (see Fig. 1), indicate that the thickness of all specimens examined here is negligible small compared to the range of these high-energy ions, thus the rate of energy transfer of the projectiles to the stopping medium can be regarded as constant in our study. The detailed discussion of the energy loss and the damaged structure along the ion path will be discussed in Sec. III C. The TEM studies were carried out using Philips-CM30 and JEOL JEM-4000EXII microscopes operated at 100 and 200 kV.

III. RESULTS AND DISCUSSION

A. Overview of the microstructure

Schematic illustration of the high-energy ion irradiation in the sample is shown in Fig. 2(a). The ion-beam direction is nearly parallel to the *c* axis of YBCO, and a low magnification TEM micrograph in plan-view of the YBCO crystal irradiated with 1.3 GeV U ions is shown in Fig. 2(b). Each black dot corresponds to a single damaged defect track induced by high-energy ions, and we can see that the distribution of ion tracks is fairly uniform in the region shown in Fig. 2(b). Defect microstructures in YBCO single crystals

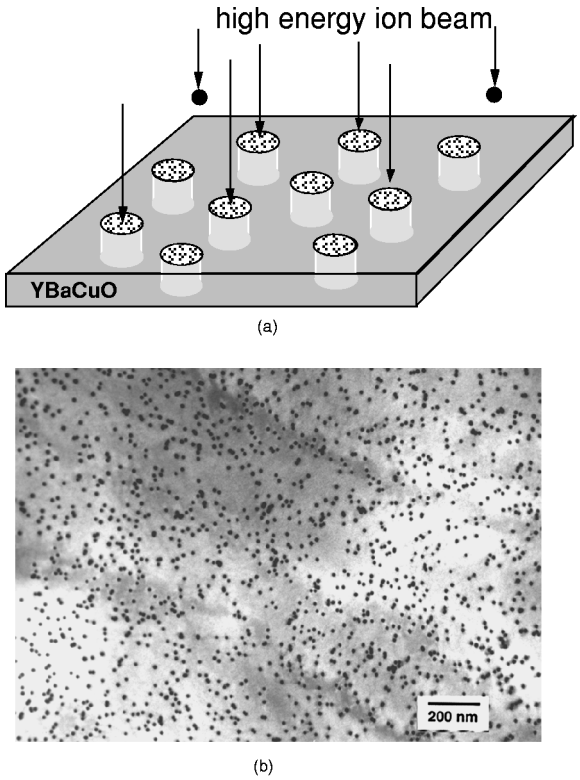

FIG. 2. (a) Schematic illustration of the high-energy ion irradiation in $YBa_2Cu_3O_{7-\delta}$. (b) Low magnification TEM micrograph in plan view of the YBCO crystal irradiated with 1.3 GeV U ions, the ion-beam direction is nearly parallel to the *c* axis of the YBCO specimen.

irradiated with three different high-energy ions are shown at higher magnification in Fig. 3. The approximately circular projections of the U, Xe, and Au ion-induced amorphized regions are readily discerned in Figs. 3(a)–3(c), and the inclined lines in Fig. 4(b) are pre-existing twin boundaries. Fig. 4(a) shows the same region as in Fig. 3(a), but as viewed about 15° away from the incident beam and recorded in bright field using the diffracting vector $g=440$ under very weak diffraction condition to minimize dynamical diffraction contrast effects. By tilting the specimen through various angles and observing the same defects, we find that the 1.3 GeV U ion irradiation produces columnar defects, which are nearly uniform in diameter and continuous throughout the thickness of the TEM sample (top 3 μm). Figure 3(b) shows typical morphology of a YBCO crystal irradiated with 2.29 GeV Xe ions at the top 10 μm part of the entry surface of the crystal. Apparently the contrast of the damaged defects in Fig. 3(b) is weaker compared to that in Fig. 3(a), and their sizes also seem varied. Figure 4(b) illustrates the same region as in Fig. 3(b), but as imaged in bright field at about 15° to the *c* axis using the diffracting vector $g=600$ under very weak diffraction condition similar to that of Fig. 4(a). One important distinction in Fig. 4(b) is the discontinuous nature of the tracks, which means that the damaged structure is not uniform along the ion path, and raises some question about the direct application of a mean electronic loss value to the description of local track formation. A plan-view micrograph of the YBCO sample by irradiation with 2.25 GeV Au ions is shown in Fig. 3(c) at a moderate magnification with apparent

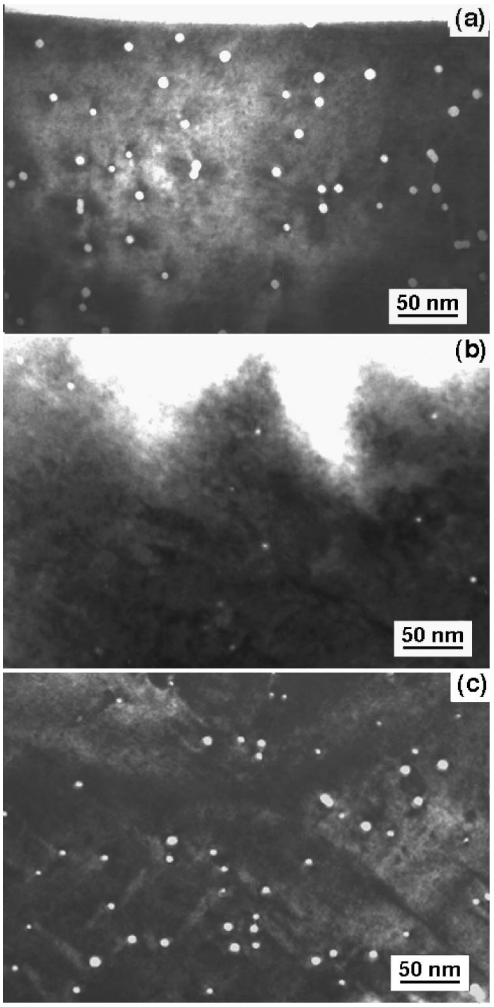

FIG. 3. TEM micrographs of an end-on view of the columnar damage in the thin foil of single crystals with (a) 1.3 GeV U, (b) 2.29 GeV Xe, and (c) 2.25 GeV Au ions.

variation of the diameter. When the area viewed away from the beam irradiation direction [Fig. 4(c)], taken in dark field at a high deviation parameter, we can now see that the columns are generally far from uniform in cross section along their lengths. The diameter variations, for a given column, are typically in the range of 4–11 nm. Moreover, the modulations in the shape along the *c* axis appear to be quasiperiodic but do not exhibit the same periodicity from column to column and can change locally on a given column. Various periods for the oscillation in diameter were seen and very few columns were apparently parallel sided. In a thin foil of a thickness which is typically 25 nm or less when examining the high resolution electron microscope (HREM) contrast of the columns along the [001] direction, the apparent diameter of any column is determined by the specific position at which it and thin foil intersect, which often has various value as shown in Fig. 3(c).

B. Local oxygen reordering

It is apparent that isolated tracks exhibit lobed ''bow-tie'' contrast along the *b* axis in the [001] ZABF image obtained using only the transmitted beam at the [001] zone axis in the samples irradiated with heavy ions. The lobed contrast is in perpendicular orientations on opposite sides of pre-existing twin boundaries [marked TB in Figs. 5(a)–5(b)]. That is, it changes from being in the horizontal direction in top left twinned domain [marked *H* in Fig. 5(a)] to the vertical direction in bottom right twinned domain [marked *V* in Fig. 5(a)] as does the direction of the *b* axis of the matrix. That the lobes lie along the *b* rather than the *a* axis was verified by the examination of dark field images at varying deviation parameters,[4,13] and the local a/b transformation was confirmed by the comparison of the form of the contrast inside and outside the lobes in high-resolution images along the [001] direction (see Fig. 7). The strength of the ''bow-tie'' contrast in the samples irradiated by different ions changes in varying degree. Figure 5(b) shows the weak lobed ''bow-tie'' contrast associated with the ion tracks having relative large diameter [marked $L1$ and $L2$ in Fig. 5(b)] in the 2.29 GeV Xe ion irradiated sample. No obvious ''bow-tie'' contrast was observed for the small-diameter amorphous track [marked $S1$ in Fig. 5(b)] in this sample.

A low magnification [001] HREM image, obtained by multi-beam with a large aperture, of the damaged tracks in the U ion irradiated sample is shown in Fig. 6(a), an imaging condition in which the 'bow-tie' contrast is relatively weak. The [001] ZABF image, obtained using the transmitted beam at the [001] zone axis, of the same region of Fig. 6(a) is

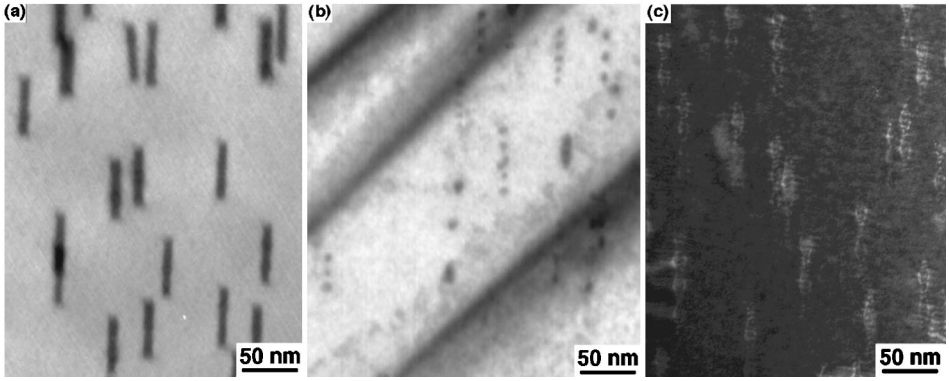

FIG. 4. TEM micrographs of a tilted ($\sim 15°$ away from the *c* axis) view of columnar damage formed by irradiation with (a) 1.3 GeV U ions imaged using the bright field, (b) 2.29 GeV Xe ions imaged using the bright field, and (c) 2.25 GeV Au ions imaged using dark field, all under very weak diffraction conditions to minimize dynamical diffraction contrast effects. Discontinuous track formation and modulated structure along the *c* axis can be seen in (b) and (c), respectively.

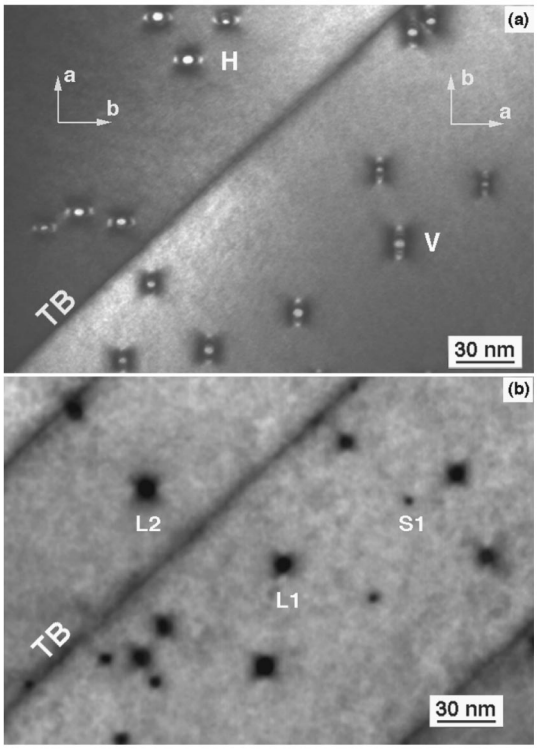

FIG. 5. An [001] zone axis bright field image showing (a) strong lobed ''bow-tie'' contrast associated with the isolated columnar defects in the YBCO crystal irradiated with 1.3 GeV U ions (Number: WMU 2003-2). Across a twin boundary (marked TB), the direction of the lobed bow-tie contrast rotates 90°. (b) Weak lobed ''bow-tie'' contrast in the YBCO crystal irradiated with 2.29 GeV Xe ions (Number: LPB-2). Across a twin boundary (marked TB), the direction of the lobed bow-tie contrast rotates 90° from the track $L1$ to $L2$. No ''bow-tie'' contrast was observed for the track with small diameter (see $S1$).

shown in Fig. 6(b). We can see that the ''bow-tie'' contrast is enhanced now. Figure 6(c) is an [001] HREM image of a typical isolated damaged track in the U ion irradiated sample. It should be pointed out that the ''bow-tie'' contrast exhibited here is not the same as the lobed contrast produced by a strain field when imaged by conventional two-beam imaging condition. In fact 200 and 020 two beam images of the damaged tracks exhibited similar Ashby and Brown[11] contrast in both these directions.[8] Therefore the strain contrast, which is parallel to the reciprocal lattice vector of the reflection used for the image in two-beam condition, does not change its orientation across a twin boundary. The contrast behavior in Figs. 5 and 6 is thus indicative of an a/b transformation of the regions adjacent to the column in the b direction of the matrix through the reordering of the oxygen atoms in the Cu-O chains. In fact, due to the oxygen reordering, a lattice fringe shift across the a/b transformation region can be seen along the direction of the small arrow labeled inside the ''bow-tie'' area in Fig. 6(c). The darker edges of the lobes in the images will, on this basis, delineate the apparently diffuse a/b interfaces where only partial reordering of the oxygen atoms on the Cu-O chains has taken place. The image in Fig. 6(d) shows damaged tracks in the Au ion irradiated sample where pre-existing twin boundaries (labeled as TB) can be seen. For this image the specimen was oriented slightly off the exact [001] direction so that one set of twinned domains is in light contrast (group $T1$), and the others are in darker contrast (group $T2$). It can be seen that the ''bow-tie'' contrast of the ORO regions around the tracks in the twinned domain $T1$ is also dark, which is similar to the neighboring twinned domains because they have the same Cu-O chain orientation. Vice versa for twinned domain $T2$, the ORO regions are in lighter contrast. Moreover the ''bow-tie'' contrast around the amorphous tracks rotates 90° after crossing a twin boundary each time in Fig. 6(d), i.e., it changes from being in the horizontal direction in twinned domains $T1$ to the vertical direction in twinned domains $T2$ as does the direction of the oxygen chains in the matrix.

An [001] HREM image of a pre-existing twin boundary [marked TB in Fig. 7(a)] with several separated damaged tracks is shown in Fig. 7(a). It is well known that there are two kinds of oxygen vacancies which are ordered in the perfect structure: one is located at $(0,0,1/2)$ in the Y planes, and the other is at $(\frac{1}{2},0,0)$. It is the latter that leads to the existence of a Cu-O chain along the b direction in the basal planes. Across a typical twin boundary such as shown in Fig. 7(a) the oxygen chains are rotated 90°. Optical diffraction patterns obtained from each of the twinned domains, right one and left one, are shown in Figs. 8(b) and 8(c) respectively. While the intensities of all {110} reflections are almost identical in both twinned domains, that of the lowest index reflections (100 and 010 here) in the right domain is much stronger along the 4-10 o'clock direction than the 2-8 o'clock direction [see Fig. 7(b)], and this exchanges in the left domain across the boundary [see Fig. 7(c)]. Pendellösung plots for (100) and (010) beams contributing to the HREM images in the [001] projection are given in Fig. 8 for an accelerating voltage of 200 kV. These show that significant differences between the (100) and (010) beams, associated with the oxygen ordering in the basal planes, are apparent when specimen thickness is greater than 7.0 nm.[4,5] Further analysis of simulated c-axis high-resolution images reveals that a distinctive contrast feature associated with the oxygen ordering can be defined as the difference in the amplitudes of the Fourier coefficients $U(010)$ and $U(100)$ of the intensity in the image.[12] Thus the intensity difference in optical diffraction across the twin boundary exhibited here is associated with the exchange of oxygen chain orientation, although precise experimental conditions, such as thickness and *defoci*, are needed in order to determine which direction is the chain direction,[12] due to the intensities of the (100) and (010) reflections that oscillate with the crystal thickness (see Fig. 8). Figure 7(d) shows an optical diffraction pattern obtained from the region between two columnar tracks [area ORO in Fig. 7(a)]. It is interesting to see that the intensity distribution of lowest index in the optical diffraction obtained from the ORO area is different from the matrix of the left twinned domain [Fig. 7(c)]. In fact the direction of stronger reflection rotates 90° from Fig. 7(c) to 7(d). As explained above this means that, in the ORO area, the oxygen atoms in the Cu-O chains have been reordered.

In addition to the lobed ''bow-tie'' contrast seen at isolated columns, defects of a more planar nature are often seen (labeled as JR in Fig. 9) and these tend to link damaged columns. An [001] HREM image showing the local ''twin'' boundary induced by two damaged tracks close together in

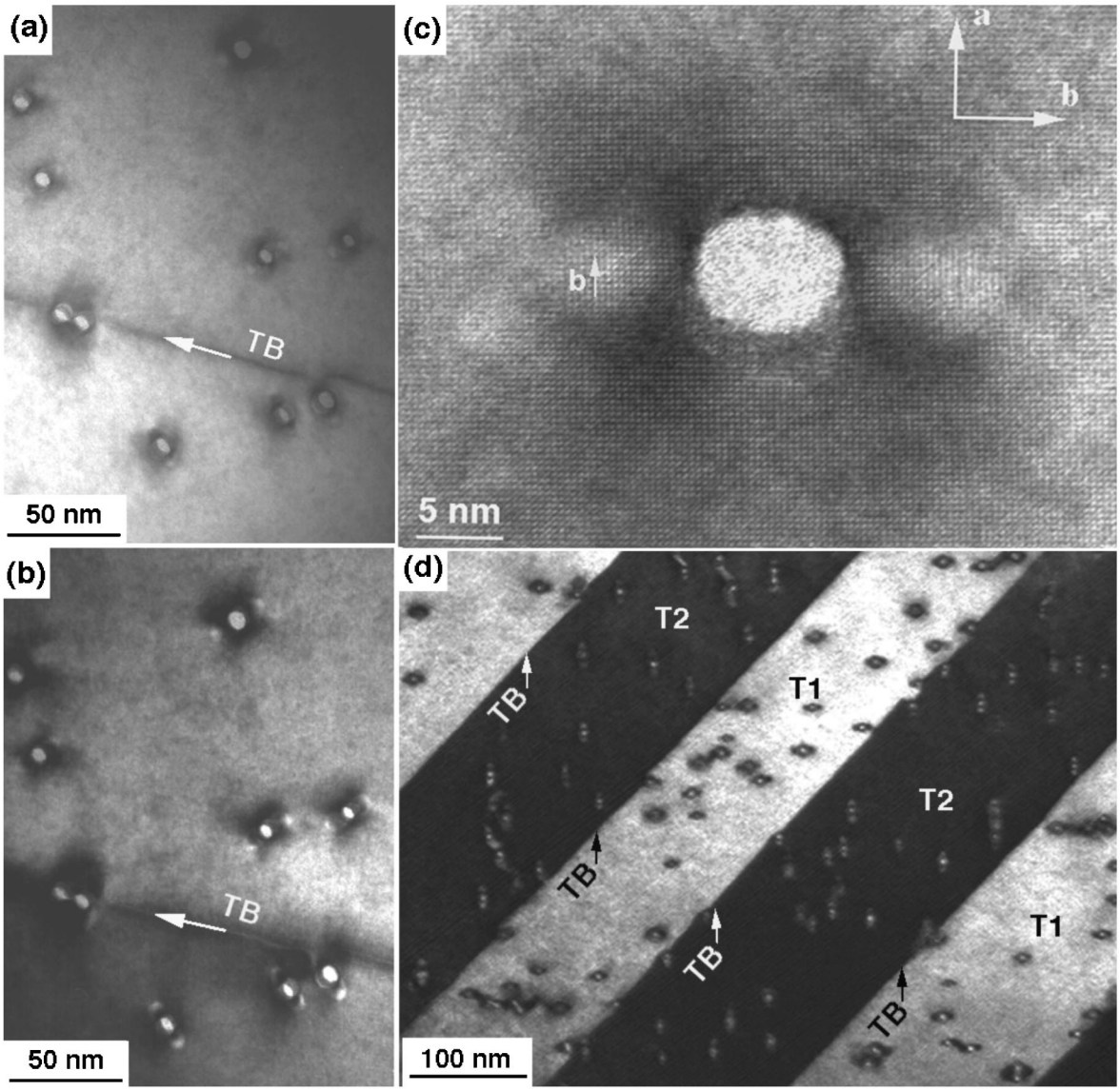

FIG. 6. (a) A low magnification [001] HREM image, obtained by multibeam with a large aperture, (b) an [001] ZABF image, obtained using only the transmitted beam at the [001] zone axis, of the same region of (a), (c) an [001] HREM image of a typical isolated damaged track in the U ion irradiated sample, and (d) TEM micrograph showing damaged tracks with several pre-existing twin boundaries (labeled as TB) in the Au ion irradiated sample. In (d) the specimen was oriented slightly off the exact [001] direction so that one set of twinned domains are in light contrast (group $T1$), and the others are in darker contrast (group $T2$). Note: the ''bow-tie'' has the contrast similar to the neighboring twinned domains because they have the same Cu-O chain orientation.

the a direction and the optical diffraction pattern of the region are shown in Fig. 10. The habit of these planar defects tends to either {110} plane even if the precise orientation is apparently constrained more by the local damage geometry than by the low energy to be expected for a perfect {110} habit. That the interfaces here are more diffuse than the preexisting twin boundaries, formed during the tetragonal to orthorhombic transformation when cooling, will also decrease the tendency for the {110} habit to be dominant. Nevertheless, the spot splitting of the $(110)/(\bar{1}10)$ reflections, as shown in the inset of Fig. 10, further confirms that the typically diffuse interface observed in Fig. 10 separates regions for which the a and b axes are exchanged and the Cu-O chain directions are reoriented by 90°. When such regions are examined using a 220 reflection their α-fringe contrast of the interface varies from place to place as a result of the varying thickness of the overlapped twinned layers.[13]

C. Model of the oxygen reordering

The driving force for the local oxygen reordering around the tracks is the strain relaxation which is enabled by replacing the shorter basal axis with the longer one of the anisotropic cell dimensions in the orthorhombic YBCO structure. That is, there is an interchange of b and a since $b>a$. It is well known that uniaxial pressure favors twinned domains that have their a axis parallel to the direction of compression and completely detwinned crystals of YBCO have been made using suitably tailored pressures and temperatures.[14] Schematic illustration for producing a detwinned YBCO single domain by an uniaxial pressure is shown in Fig. 11.

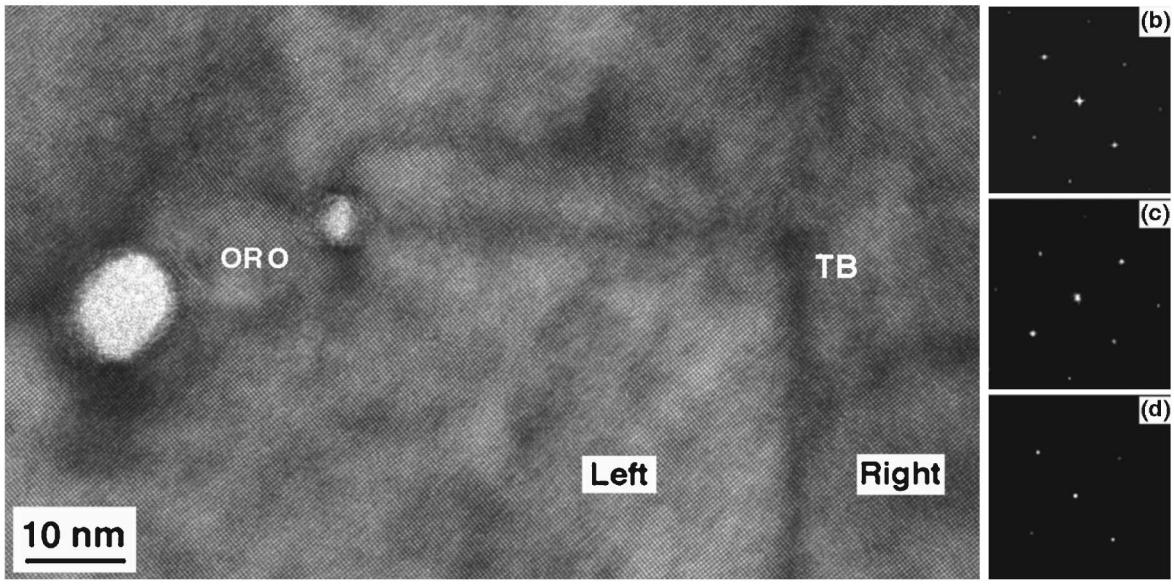

FIG. 7. HREM image of the YBCO crystal irradiated with 2.25 GeV Au ions showing a pre-existing twin boundary (marked TB) with a few damaged tracks (a). Optical diffraction patterns from the right twinned domain (b), the left twinned domain (c), and oxygen reordering (marked ORO) region (d).

As explained in more detail in Fig. 12, the uniaxial pressure entails 90° reorientation of the oxygen chains in twinned domains $T1$ with their b axes parallel to the direction of compression [see Fig. 12(a)]. However, there is no change in twinned domains $T2$ having their a axes parallel to the compression [see Fig. 12(b)].

We suggest that the process of local oxygen reordering we observe here in irradiated YBCO is of an analogous origin. In the very high ion energy regime as examined here, the dominant mode of energy transfer from fast ions to the target lattice in the first part of the damage track is electronic ionization and excitations. Fast ion energy losses through nuclear collisions with target atoms are at least two orders of magnitude smaller. Hence the defect formation mechanism is thought to rely largely on the magnitude of the local ionization density. Before the time of electronic recovery of the

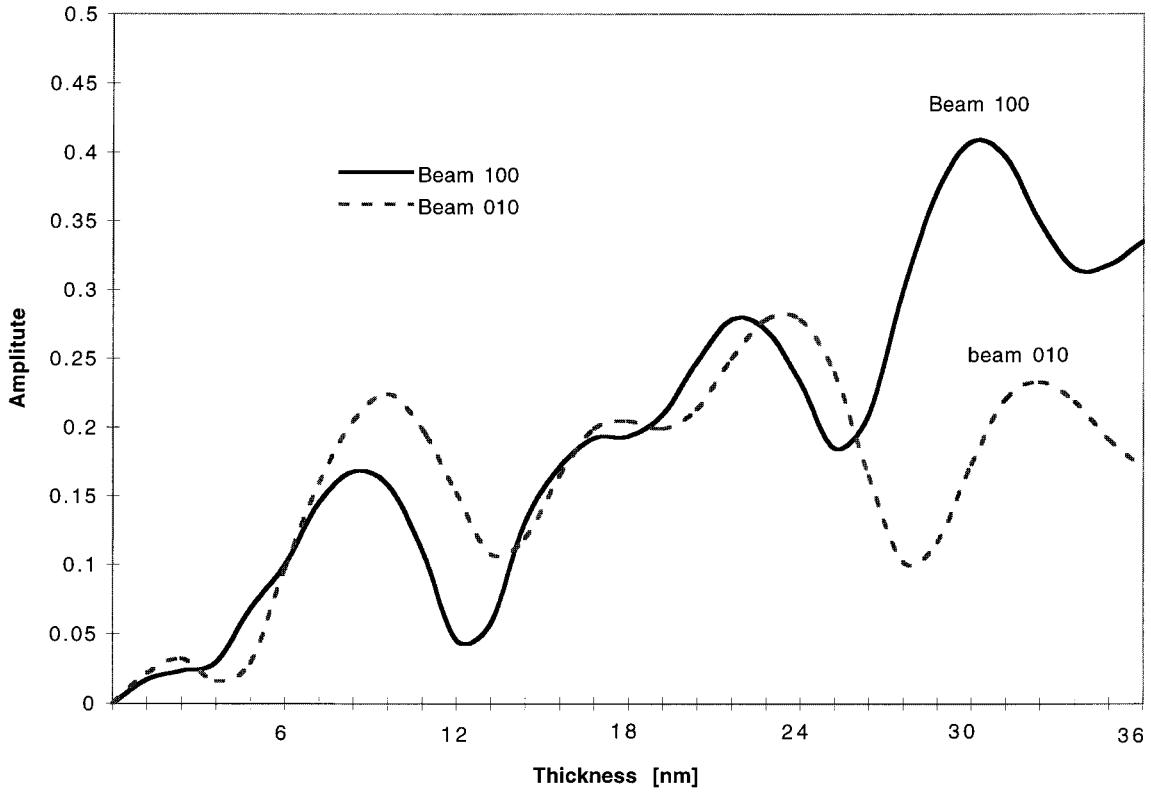

FIG. 8. Pendellösung plots for (100) and (010) beams contributing to the HREM images in the [001] projection.

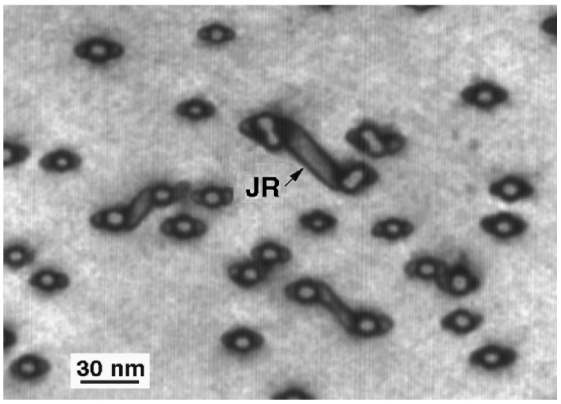

FIG. 9. An [001] zone axis bright field image showing parallel planar defects on {110} associated with two or more tracks in the YBCO crystal (Number: WMU 2003-2) irradiated with 1.3 GeV U ions. Note that the lobed bow-tie contrast of an isolated track is along the *b* axis of the matrix, but the boundaries of the joint oxygen reordered regions (labeled as JR) are in either {110} plane.

highly ionized cylinder of material along the ion path, the Coulomb repulsion results in local expansion and a surrounding compressive stress. This time is sufficient to result in the formation of an amorphous structure approximately inside the ionization cylinder, and the reordering of oxygen in a volume outside the amorphous cylinder. This would be consistent with the observed shapes of the ORO regions on the above basis that pressure along the *b* axis can be relieved in this manner.

For simplicity we first only consider the region along the *a* or *b* axis around a damaged track. Schematic illustration showing the stress fields are reduced by the local oxygen reordering in these regions is given in Fig. 13. Suppose that the original point *O* is at the center of the track, and the *X* and *Y* directions of the coordinate are parallel to the *b* and *a* axes of the crystal [see Fig. 13(a)] respectively. Before the irradiation the unit cells (the ratio a/b is enlarged for better display) are distributed uniformly in both the *X* and *Y* directions. After an ion passed at the point *O*, an amorphous core is formed and the cylindrically symmetric compressive field around the amorphized central core of the damage track produces a uniaxial pressure in the region along the *X* and *Y* directions under which the unit cells in the both region would be highly deformed [see Fig. 13(b)]. Now the situation in the region along the *X* and *Y* directions in Fig. 13(b) are similar to that in the twinned domains $T1$ and $T2$, respectively in Figs. 11 and 12. Thus the *a* and *b* axes are exchanged in the region along the *X* direction that results in a local 90° reorientation of the Cu-O chains, and the unit cells in the *Y* direction remain the same crystallographic orientation [see Fig. 13(c)]. It should be noted that both a radially compressive stress as well as a tensile hoop stress can be relaxed by the reorientation of the orthorhombic unit cell not only within the transformed regions [the left or right area next to the track in Fig. 13(c)] but also in the untransformed regions [the top or bottom area next to the track in Fig. 13(c)] perpendicular to these.

As demonstrated in HREM image of Fig. 6, the habit of the a/b boundaries on both sides of the ''bow-tie'' contrast

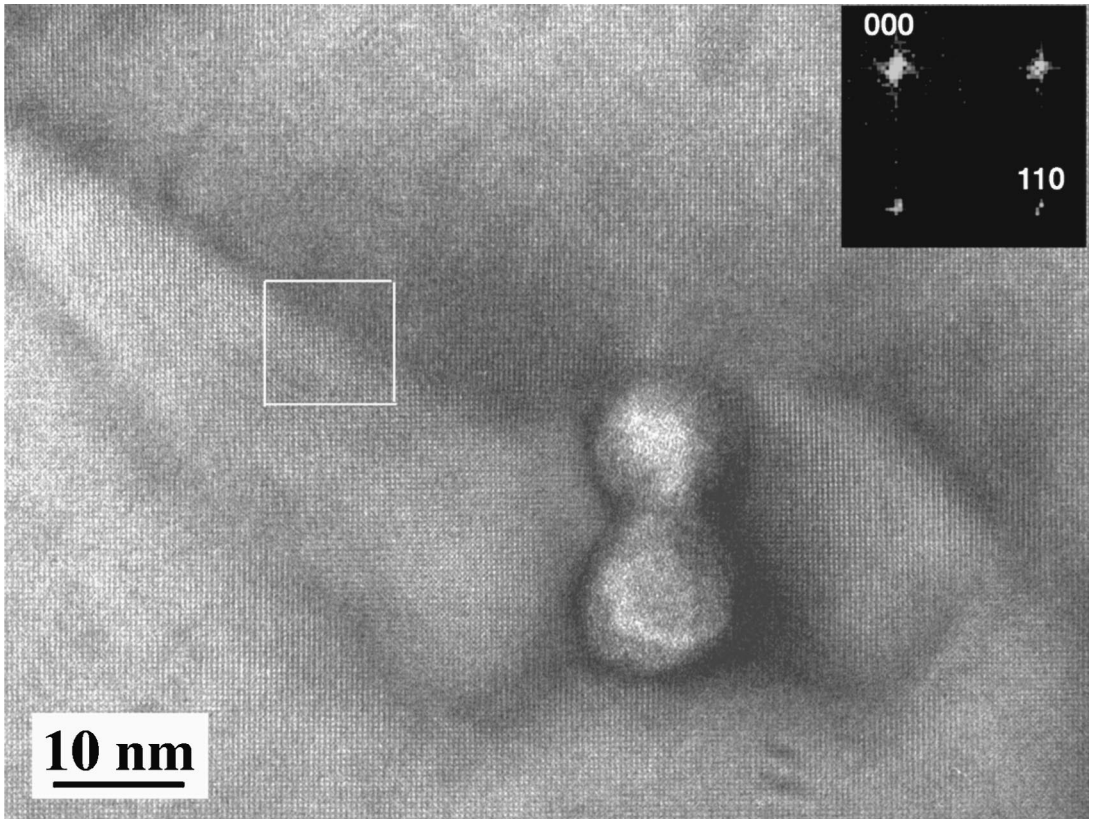

FIG. 10. An [001] HREM image showing the local ''twin'' boundary induced by two damaged tracks close together in the *a* direction in the YBCO crystal irradiated with 2.25 GeV Au ions. The inset is an optic diffraction pattern taken across the local ''twin'' boundary (Marked by a white square) that displays splitting of the 110 reflection.

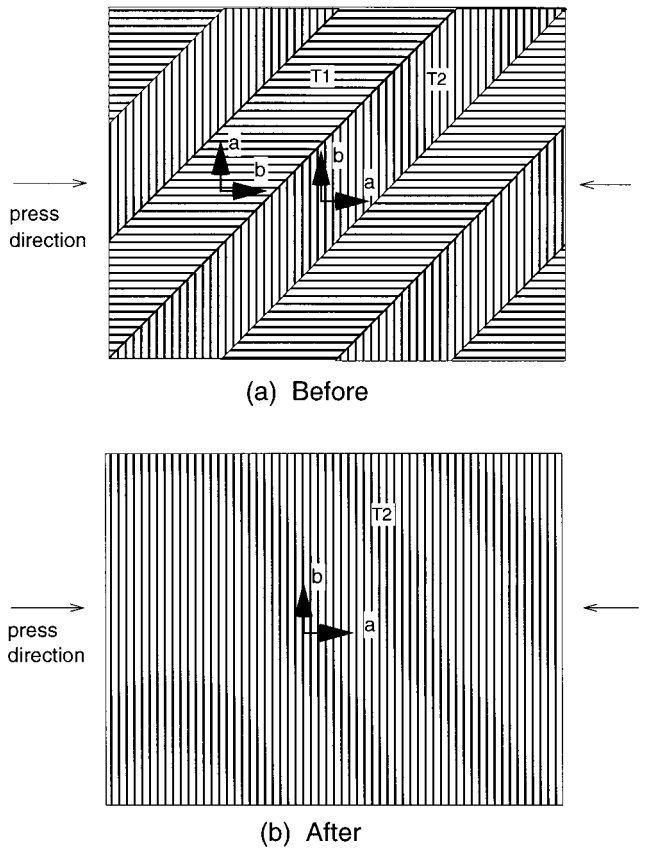

FIG. 11. Schematic illustration for producing a detwinned YBCO single domain by an uniaxial pressure.

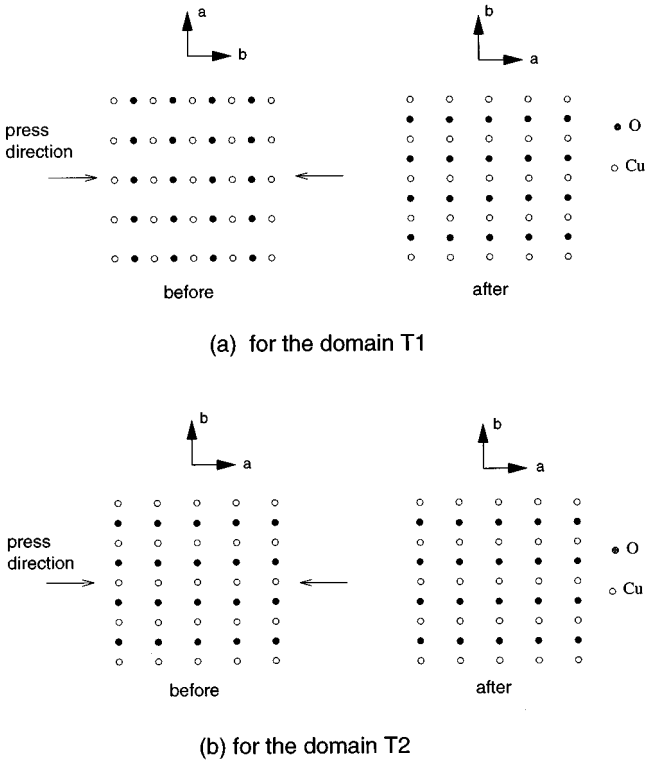

FIG. 12. (a) Uniaxial pressure entails 90° reorientation of the oxygen chains in twinned domains $T1$ of Fig. 11(a) with their b axes parallel to the direction of compression. (b) The uniaxial pressure makes no change to the orientation of the oxygen chains in twinned domains $T2$ of Fig. 11(b) having their a axes parallel to the compression.

around the amorphous track tends to either {110} plane. A general case needs to be considered to interpret such a contrast. Consider the damaged region as a large thin crystal plate having a small circular amorphous core subjected to uniform pressure, as shown in Fig. 14. Let the origin of polar coordinates be placed at the center point of the amorphous core. Assuming c direction independence for this thin plate (we will discuss it later), and the r direction ($\theta=0°$) in the polar coordinates to be along the b axis of crystal matrix. We will not try to have a quantitative solution to the strain-displacement equations for the problem due to the existence of oxygen reordering around the track that makes it even more complicated in the orthorhombic system. However, one may have a qualitative result for the ''bow-tie'' contrast shown in Figs. 5 and 6 by analyzing the force applied to the unit cells in the affected area. The stresses are clearly symmetrical about the a and b axes (one just needs to have an analysis for $\theta=0-90°$), and the deformations likewise display θ dependence. As shown in Fig. 14, an element of area ΔS, located at the point (r,θ) is acted on by force F. Decomposing F into components parallel to the a and b axes (the inset of Fig. 14), we have

$$F_a = F \sin\theta, \tag{1a}$$

$$F_b = F \cos\theta. \tag{1b}$$

Clearly F_b is larger than F_a when the element of area ΔS is located at the region of $\theta<45°$, and this would favor the formation of local oxygen reordering. For $45°<\theta<90°$, F_b is smaller than F_a and the oxygen chains would not change their direction. Thus the a/b boundaries on both sides of the amorphous track tend to either {110} plane which is in fact also a low-energy twin boundary in the YBCO system.

Schematic illustration for the ''bow-tie'' contrast around the track due to the stress field relaxed by the a/b transformation in the regions with $-45°<\theta<45°$ and $135°<\theta<225°$ is shown in Fig. 15. As the distance to the origin r increases, the force F is reduced that will limit the oxygen reordering to a certain area next to the amorphous core. Experiment observations indicate that the size of the ORO area is about 10 nm to each side of an isolated track with diameter 10 nm (see Figs. 5 and 6). As indicated earlier, the Cu-O chain direction rotates 90° across a pre-existing twin boundary in the orthorhombic YBCO crystal. Thus it is not surprising to see that the lobed bow-tie contrast around an isolated track in Fig. 5(a) changes direction from horizon to vertical, a schematical drawing of which is shown in Fig. 16. That the stress field is not fully relaxed by the a/b transformation is only in part due to the geometry and will be strongly affected by the time constants for the decay of the local temperature around the amorphized region, which will differ as a function of the rate of energy release and the ion speed. This interpretation is consistent with the diffuse nature of the interfaces of the transformed regions.

In addition to the lobed a/b interfaces around isolated columns, defects of a more planar nature are also observed

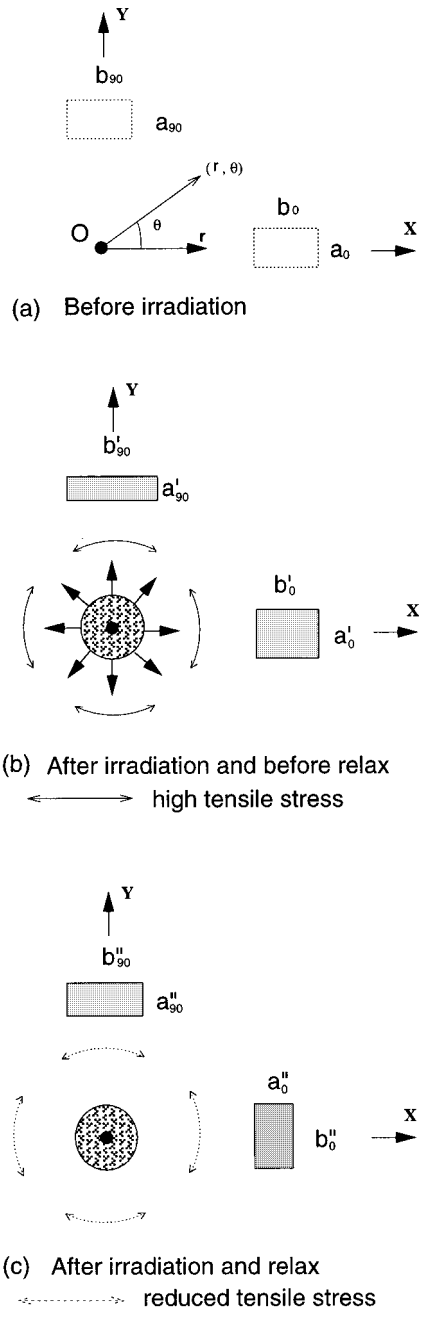

FIG. 13. Schematic illustration showing how the stress fields can be reduced by the local oxygen reordering in the surrounded regions along the a and b axes of the matrix: (a) before the irradiation, (b) after the irradiation and before relaxing of the stress, and (c) after irradiation and relaxing of the stress.

and these tend to link damaged columns. This in itself emphasizes the fact that the relaxation process described for a given isolated column is incomplete. Thus the joining of the transformed regions will occur after the second of a given pair of tracks is formed. Again the habit of these boundaries of transformed regions tends to either {110} plane. As long as the ORO mechanism for an isolated track is established, the model for the ORO region formed between two columns is rather simple. It appears that this is just a modification of the relaxation process described above for the isolated columns. The more complicated geometry of the a/b boundaries is

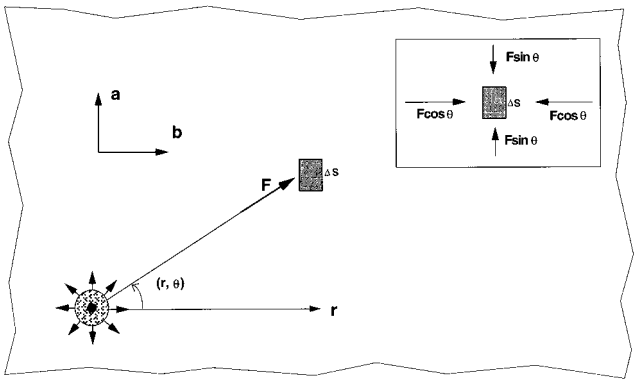

FIG. 14. A large thin crystal plate having a small circular amorphous core subjected to uniform pressure in polar coordinates. The inset shows an enlarged area ΔS with components of the force F.

now the result of the more complex stress fields to be relaxed when the damaged columns are close together and at random orientations to one another in relation to the ⟨110⟩ directions in the crystal. Consider the damaged region having two amorphous tracks located at O and O' separated by a distance L, as shown in Fig. 17. Let the origin of the coordinates be placed at point O, the center of the left amorphous core, and the r direction in the polar coordinates to be along the Cu-O chain direction, i.e., the b axis, of the crystal matrix. As indicated earlier, around a track only the area distributed between the {110} planes (see dashed lines in Fig. 17) along the b axis of the matrix is in favor of the oxygen reordering. Thus the regions favoring oxygen reordering around the two single tracks are overlapped in the rectangle $OMO'N$ in Fig. 17, and generally between two damaged tracks the oxygen reordering can only happen in these overlapped regions. From Fig. 17, we obtain

$$OM = L\ \cos(45-\theta), \tag{2a}$$

$$ON = L\ \sin(45-\theta), \tag{2b}$$

$$S = L^2\ \sin(45-\theta)\cos(45-\theta), \tag{2c}$$

where the lines OM and ON are the lengths of long side and short side of the rectangle $OMO'N$, L is the distance between two tracks, S is the surface area of the rectangle $OMO'N$, and θ is the angle between the polar axis r (also the b axis of the matrix) and the line OO' (the linking line of the center points of the two tracks). Using natural trigonometric functions Eqs. (2a)–(2c) can be modified as

$$OM = L[\cos\ \theta + \sin\ \theta]/\sqrt{2}, \tag{3a}$$

$$ON = L[\cos\ \theta - \sin\ \theta]/\sqrt{2}, \tag{3b}$$

$$S = L^2\ \cos 2\theta/2. \tag{3c}$$

From Eqs. (3a)–(3c), one can see that when the θ decreases in the range of $0 < \theta < 45°$ the length of the long side OM is close to the short side ON and the rectangle $OMO'N$ becomes a perfect square for $\theta = 0$. On the other hand when the θ increases the difference between the long side OM and short side ON is increased, and the overlapped region disappears for $\theta = 45°$ (the short side ON is equal to zero) for

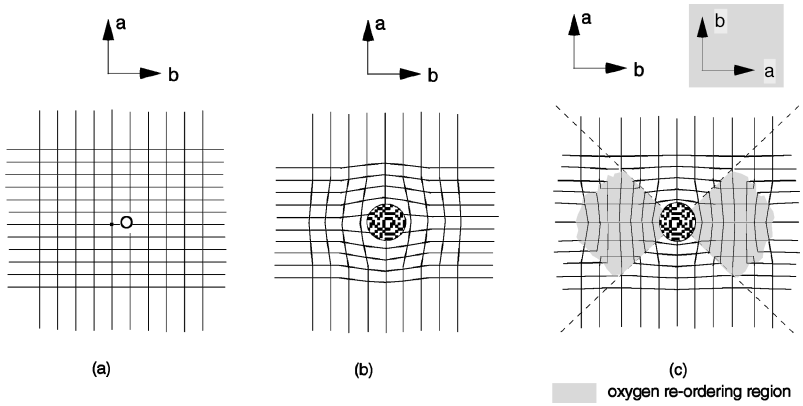

FIG. 15. Schematic illustration for the ''bow-tie'' contrast around the damaged track due to the stress field relaxed by the a/b transformation: (a) before the irradiation, (b) after the irradiation and before relaxing of the stress, and (c) after irradiation and relaxing of the stress.

which no joint ORO area between the two tracks is formed. Thus the relative orientation and the distance between two columnar tracks are crucial for the distribution of the oxygen ordering of the region between them. The magnitude of the ORO area between the two tracks S depends on both L and θ [see Eq. (3c)]. TEM observations shows that the L value is relatively small when the θ is close to zero, and it becomes larger when the θ is in the higher angle range of $0\sim45°$. When the right track is located lower than the left one in Fig. 17, i.e., $-45°<\theta<0$, the long side and the short side of the rectangle $OMO'N$ exchanges. While the ORO region is limited to ~10 nm around an isolated track as shown in Figs. 5 and 6, TEM observations indicate that the maximum ORO distance between two tracks can extend over 40 nm.

Schematic diagrams showing how the transformation of approximately parallel sided (110) planar faults (again by local internal rearrangement of the oxygen in the Cu-O chains) might relax the stress between adjacent amorphous columns in appropriate relative orientations are shown in Fig. 18. Figure 18(a) exhibits two tracks having an angle, between the linking line of the two tracks (the line OO' in Fig. 17) and the b axis of the matrix, $\theta>45°$, and one can see that the shadow regions, where the oxygen reorders for each single track, are not overlapped in Fig. 18(b). Thus there will not be a joint ORO region between them, as shown in Fig. 18(c). On the contrary, Fig. 18(d) shows another two tracks with $\theta<45°$ and the shadow regions (i.e., the ORO region) of the two tracks are overlapped now [see Fig. 18(e)], thus one would expect to see an area with the ORO region linked between them, as shown in Fig. 18(f).

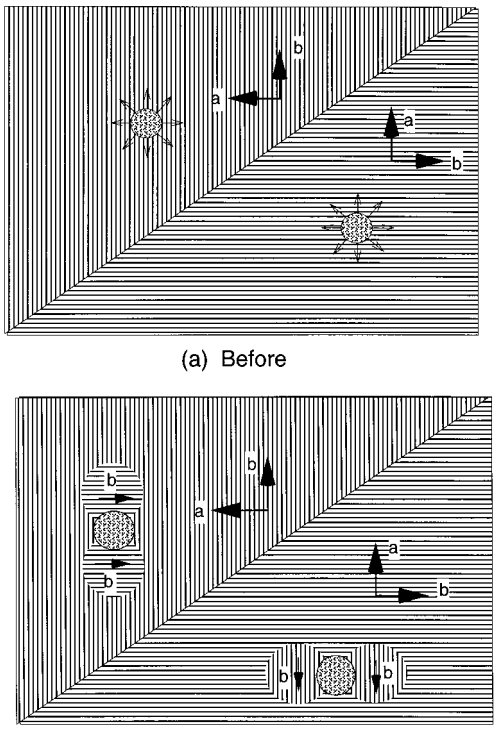

FIG. 16. Schematic illustration for the rotation of the ''bow-tie'' contrast across a pre-existing twin boundary in the high-energy ion irradiated YBCO: (a) before relaxing, (b) after relaxing.

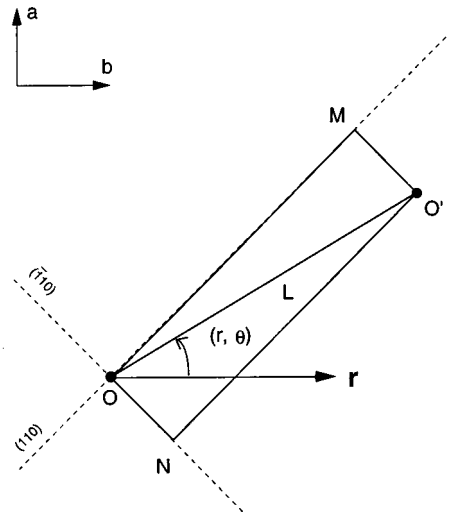

FIG. 17. Damaged region having two amorphous tracks located at O and O' separated by a distance L. Assume the origin of the coordinates to be placed at point O and the r direction in the polar coordinates to be along the b axis of crystal matrix, as labeled in the figure.

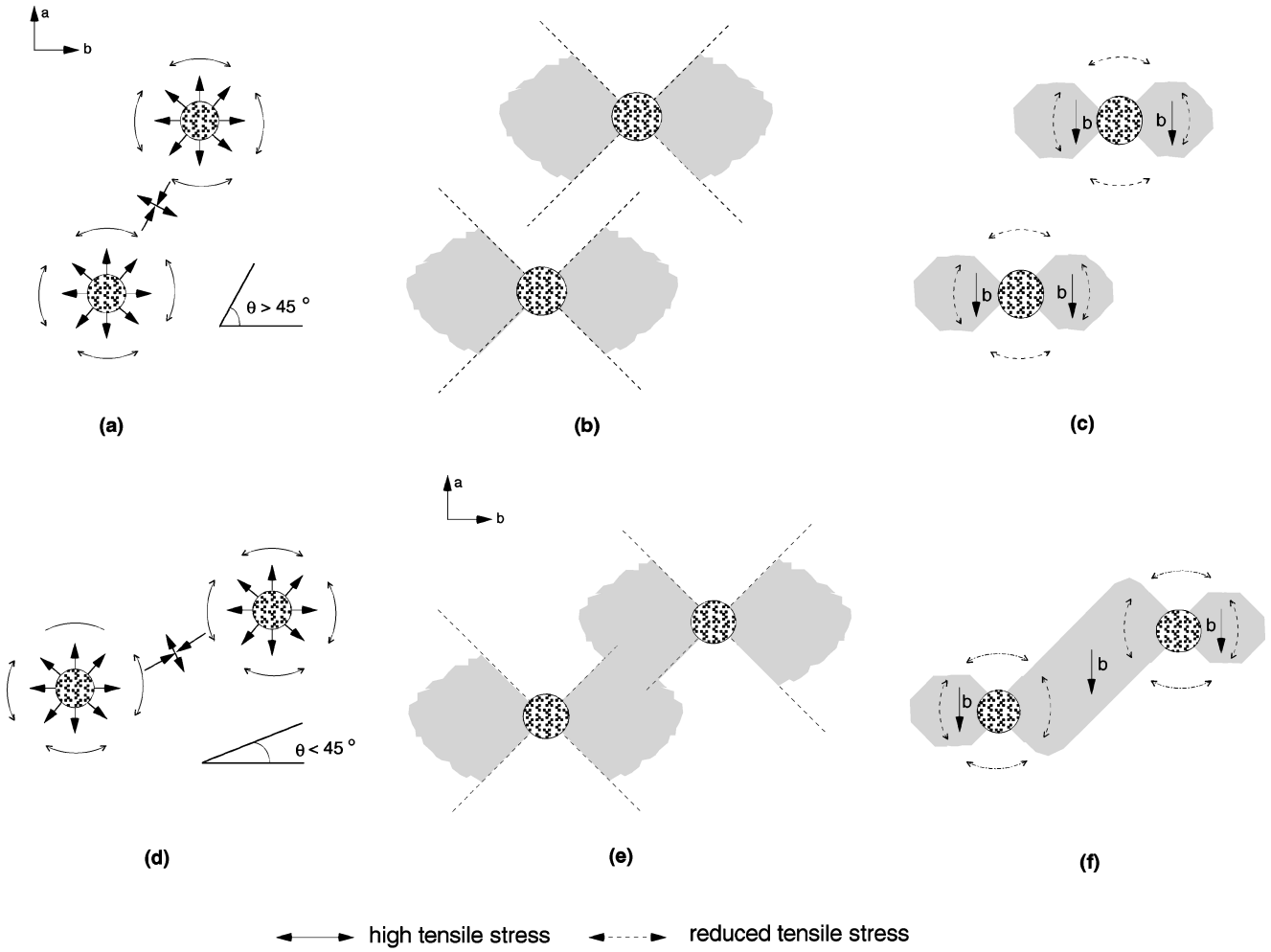

FIG. 18. Schematic diagrams showing how the local internal rearrangement of the oxygen in the Cu-O chains might relax the stress between adjacent amorphous columns in appropriate relative orientations: (a)–(c) showing two tracks with $\theta \geqslant 45°$, and (d)–(f) showing another two tracks with $\theta < 45°$. See the text for details.

The models proposed above have been confirmed by TEM experimental observations. The image in Fig. 19(a) shows several tracks in the Au ion irradiated sample with 2.25 GeV where a pre-existing twin boundary (labeled as TW) can be seen. For this image the specimen was oriented slightly off the exact [001] direction as we did for Fig. 6(d) so that the left twinned domain is in darker contrast. It has been found that the contrast of the ORO regions around the tracks in the right twinned domain is also dark, which is similar to the left twinned domain because they have the same Cu-O chain orientation. Vice versa for left twinned domain, the ORO regions are in lighter contrast. Joining of the ORO regions have been observed between the tracks N_2-N_3, N_3-N_4, M_1-M_3, and M_2-M_3 in Fig. 19(a), for which the θ (the angle between their linking lines of a pair of tracks and the b axis of the matrix) is smaller than 45°. However, there is no ORO region formed between the tracks M_3 and N_3 due to θ being higher than 45°, although the distance between them is shorter than that between the tracks N_2 and N_3. It is also interesting to see that there is a light lobed area between two closed tracks M_1 and M_2 that has a similar form to the dark area between N_1 and N_2, both of these tracks have nearly the same distance of separation, i.e., $M_1M_2 \approx N_1N_2$, but a different orientation to the Cu-O chain direction of the matrix. The line M_1M_2 is perpendicular to the b axis of the right twinned domain, and the line N_1N_2 is approximately parallel to it. Schematic diagrams showing how local internal rearrangement of the oxygen in the Cu-O chains relaxes the stress between these adjacent amorphous columns are given in Fig. 19(b) and 19(c). Usually the ORO regions between two tracks will not overlap each other when the $\theta > 45°$, as seen for the tracks M_3 and N_3. However, if the two tracks are very close (about $\leqslant 15$ nm) like the M_1 and M_2 in Fig. 19(a), the joining of the ORO areas might happen between them in the way described by Fig. 19(c).

In the discussion above we treated the damaged structure system in two dimensions, which means we assumed the damaged tracks were uniform along the c axis. However, as shown in Figs. 4(b) and 4(c), the tracks are not uniform along the ion path and they could be modulated [Fig. 4(c)] or even discontinuous [Fig. 4(b)]. Similar results have been obtained in 1.4 GeV Br^+ and 580 MeV Sn^+ irradiated YBCO sample.[15] As indicated earlier, in the very high-energy regime we used here, the dominant mode of energy transfer from fast ions to the target is through electronic ionization and excitations. The defect formation mechanism should rely largely on the magnitude of electron energy loss S_e of the incident ions. Without consideration of possible mass and velocity dependence, a threshold value T_e in the electronic stopping power, as proposed for magnetic insulators,[16] may

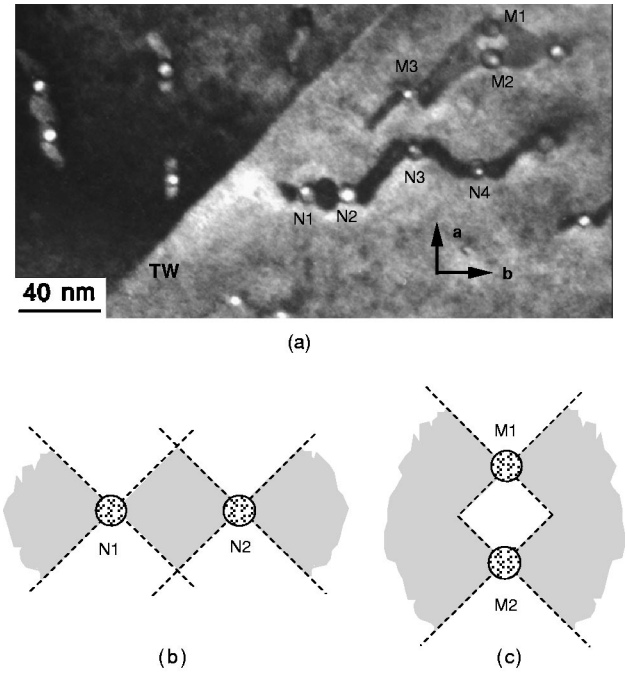

FIG. 19. (a) TEM micrograph showing several tracks in the Au ion irradiated sample with 2.25 GeV where a pre-existing twin boundary (labeled as TW) can be seen. Schematic diagrams showing how the dark contrast between the tracks N_1 and N_2, and the light contrast between the tracks M_1 and M_2 can be formed by the local oxygen reordering are shown in (b) and (c), respectively. The shadow regions correspond to the ORO areas. See the text for details

exist above which a rapid increase in the damage formation efficient in high-T_c $YBa_2Cu_3O_{7-\delta}$ occurs. TEM examinations suggested that the T_e value is about 11 keV/nm in $YBa_2Cu_3O_{7-\delta}$,[6,15] below which widely separated spherical damage regions were formed along the ion path.[15] As the electronic energy loss becomes higher, the density of damage along the ion path length is increased and continuous tracks are formed. Calculations of Fig. 1 using TRIM Monte Carlo energy deposition routine[17] show that thickness ranges used for our TEM examinations at 52 keV/nm for the U^+, 23 keV/nm for the Xe^+, and 42 keV/nm for the Au^+, as here indicated in Fig. 1 by arrows. In those ranges the magnitude of corresponding S_e, which is the determining factor in terms of the track formation, is mostly close to the threshold value T_e for Xe^+ and far above T_e for Au^+ and U^+. Thus columnar defects along the ion path are discontinuous at 23 keV/nm for the Xe^+, they become entirely continuous with modulated diameters at 42 keV/nm for the Au^+ and finally more uniform at 52 keV/nm for the U^+. Presumably the form and the size of the ORO around the damage track result from the cylindrically symmetric compressive field around the amorphized core. The magnitude of the compressive fields is associated with the volume expansion caused by amorphisation at the moment the ion just passes through. Both the magnitude of the local stress and the volume of the amorphous phase is decided by the electronic energy deposit S_e. Thus it is not surprising that the ORO effect in the 2.29 GeV Xe^+ irradiated YBCO sample is much less than in the 2.25 GeV Au^+ and 1.3 GeV U^+ irradiated samples in the observed thickness range here [see Figs. 5(a) and 5(b)].

Moreover point defect and local oxygen content variation might be induced in the surrounding area of the damaged track. Electron energy loss spectroscopy has been applied to study local electronic structures in ion irradiated[7] and electron beam irradiated[19] YBCO samples. A decrease in the empty density-of-states related to the holes responsible for electrical conduction in this materials has been observed. However, the change observed, at least for electron beam irradiated sample, is not simply related to the depletion of mobile chain oxygen as in the case of oxygen deficient YBCO compounds.[20] Our study shows that the oxygen content in the surrounding area of the damaged tracks, where the ''bow-tie'' contrast associated with reorientation of oxygen chains in orthorhombic structure was observed, should be at least as high as the value ($x \geqslant 6.4$) for which the orthorhombic structure could be formed in YBCO compounds.

IV. SUMMARY

The damaged structures have been systematically studied in the present high-energy ion irradiated $YBa_2Cu_3O_{7-\delta}$ superconductors. The irradiation with 2.25 GeV Au and 1.3–1.4 GeV U ions results in the formation of highly aligned defects, which are usually amorphous and the associated volume expansion causes strain in the surrounding matrix. The diameters of the tracks vary along the c axis depending on the magnitude of the electronic energy loss. Characteristic lobed ''bow-tie'' contrast features along the b axis of the matrix, which are caused by local oxygen reordering in the ab planes to give a 90° reorientation of the orthorhombic unit cell in the affected area, have been studied in both the [001] HREM and ZABF images. The typical value of the ORO area for an isolated amorphous core (diameter: ~10 nm) is about 10 nm, and it could extend over 40 nm in the area between adjacent two amorphous columns. The driving force of the formation of the oxygen reordering comes from a cylindrically symmetric compressive field, which would be expected to occur after the ion has passed, around the amorphized damage track caused by the electronic energy loss. This uniaxial pressure on the orthorhombic YBCO structure favors the local rearrangement of the oxygen in the Cu-O chains in the region along the [010] direction of the matrix around the track due to pressure along the b axis that can be relieved in this manner. Detailed analyses indicate that the lobed a/b interfaces tend to be in either of the {110} planes, the angle between which and the Cu-O chain direction, θ, is 45°. The lobed contrast for the sample irradiated by the 2.29 GeV Xe ion at energy loss ~23 keV/nm is much weaker than irradiated by 1.3 GeV U^+ at energy loss ~52 keV/nm and 2.25 GeV Au^+ at energy loss ~42 keV/nm [see Figs. 5(a) and 5(b)], since the average track diameter produced by 2.29 GeV Xe ions at the ranges examined is smaller than the others [see Figs. 3(a)–3(c)].

The joining and developing of the ORO regions between adjacent tracks, occurring after the second of a given pair of closed tracks is created, tend to be formed in the overlapped region of the ORO favoring area of each single track. The form of the rectangular ORO area between two or more tracks is usually decided by the relative orientation of the tracks to the Cu-O chain direction. When θ (the angle between the b axis of the matrix and the linking line of the

center points of the two tracks) is greater than 45°, the joint ORO area between the two tracks would disappear since the ORO favored regions around each of the two tracks will not overlap each other.

Flux pinning from radiation damage in high T_c superconductors is ascribed to local regions where the superconductivity is weakened, so that the energy cost of locating a flux line in this region is reduced.[1] The system, therefore, gains an amount of condensation energy $U_p = \eta(H_c^2/8\pi)\nu$.[18] Where $\eta \leqslant 1$ is the fractional suppression of superconductivity in the defects, H_c is the thermodynamic critical field, and ν is the volume of the vortex core that is pinned. The volume of nonsuperconducting material produced by heavy-ion irradiation is normally taken to be the amorphized column as well as, to a degree, the strained surrounding regions in which the superconductivity will also be suppressed. Along the field direction, ν is limited by the greater of coherence length ξ or the defect size.[1] This in turn suggests that it should be important to assess the relevance in this context of the diffuse ab boundaries associated with the oxygen reordering seen in this study. It is also important to take the modulation and continuity of the damaged structures along the ion path, which vary with magnitude of the electronic energy loss, into account when calculating the volume ν. Detailed study of distribution of the damaged structure along the ion irradiation direction is under the way and will be reported in the near future.

ACKNOWLEDGMENTS

The authors are indebted to Dr. L. Paulius (Western Michigan University), Dr. W. Kwok (Argonne National Laboratory), and Dr. G. Wirth (Gesellschaft fur Schwerionenforschung) for providing irradiated YBCO samples. This work was supported by the U.S. Department of Energy under Contract No. W-31-109-ENG-38.

[1] L. Civale, A. D. Marwich, T. K. Worthington, M. A. Kirk, J. R. Thompson, L. Krusin-Elbaum, Y. Sun, J. R. Clem, and F. Holtzberg, Phys. Rev. Lett. **67**, 648 (1993).

[2] M. A. Kirk, Mater. Res. Soc. Symp. Proc. **209**, 743 (1991).

[3] R. A. Doyle, W. S. Seow, Y. Yan, A. M. Campbell, T. Mochiku, K. Kadowaki, and G. Wirth, Phys. Rev. Lett. **77**, 1155 (1996).

[4] Y. Yan, R. A. Doyle, A. M. Campbell, G. Wirth, and W. M. Stobbs, Philos. Mag. Lett. **73**, 299 (1996).

[5] W. Gerhauser, G. Ries, H. W. Neumuller, W. Schmidt, O. Eibl, G. Saemann-Ischenko, and S. Klaumunzer, Phys. Rev. Lett. **68**, 879 (1992).

[6] V. Hardy, D. Groult, M. Hevieu, J. Provost, and B. Raveau, Nucl. Instrum. Methods Phys. Res. B **54**, 472 (1991).

[7] Y. Zhu, Z. X. Cai, B. C. Budhani, M. Suenaga, and D. O. Welch, Phys. Rev. B **48**, 125 (1993).

[8] Y. Zhu, Z. X. Cai, and D. O. Welch, Philos. Mag. A **73**, 1 (1996).

[9] D. O. Welch, Y. Zhu, and B. C. Budhani, in *Critical State in Superconductors*, edited by K. Tachikawa, K. Kitazawa, H. Maeda, and T. Matsushita (World Scientific, Singapore, 1995), p. 221.

[10] M. C. Frischherz, M. A. Kirk, J. Farmer, L. R. Greenwood, and H. W. Weber, Physica C **232**, 309 (1994).

[11] M. F. Ashby and L. M. Brown, Philos. Mag. **8**, 1083 (1963).

[12] Y. Yan, W. Y. Liang, T. Walther, and W. M. Stobbs, Phys. Rev. B **54**, 16 234 (1996).

[13] Y. Yan, R. A. Doyle, W. S. Shew, A. M. Campbell, G. Wirth, and W. M. Stobbs, Inst. Phys. Conf. Ser. **147**, 433 (1995).

[14] U. Welp, M. Grimsditch, H. You, W. K. Kwok, M. M. Fang, G. W. Crabtree, and J. Z. Liu, Physica C **161**, 1 (1989).

[15] R. Wheeler, M. A. Kirk, A. D. Marwick, L. Civale, and F. H. Holtzberg, Appl. Phys. Lett. **63**, 1573 (1993).

[16] F. Studer and M. Toulemonde, Nucl. Instrum. Methods Phys. Res. B **65**, 560 (1992).

[17] J. F. Ziegler, J. P. Biersack, and U. Littlemark, *The Stopping and Range of Ions in Solids* (Pergamon, New York, 1985).

[18] A. M. Campbell and J. E. Evetts, Adv. Phys. **21**, 199 (1972).

[19] J. Yuan, Y. Yan, and A. Pauza, Inst. Phys. Conf. Ser. **147**, 429 (1995).

[20] N. D. Browning, J. Yuan, and L. M. Brown, Semicond. Sci. Technol. **4**, 346 (1991).